Experimental Evidence for Self-Assembly of CeO2 Particles in Solution: Formation of Single-Crystalline Porous CeO2 Nanocrystals

6 AUTHORS, INCLUDING:

Thomas W. Hansen
Technical University of Denmark
114 PUBLICATIONS **1,724** CITATIONS

Ming Lin
Agency for Science, Technology and Researc…
56 PUBLICATIONS **1,388** CITATIONS

Experimental Evidence for Self-Assembly of CeO₂ Particles in Solution: Formation of Single-Crystalline Porous CeO₂ Nanocrystals

Hui Ru Tan,[†] Joyce Pei Ying Tan,[†] Chris Boothroyd,[‡,§] Thomas W. Hansen,[‡] Yong Lim Foo,[†] and Ming Lin[*,†]

[†]Institute of Materials Research and Engineering, A*STAR (Agency for Science, Technology and Research), 3 Research Link, S117602, Singapore

[‡]Center for Electron Nanoscopy, Technical University of Denmark, DK-2800 Kongens Lyngby, Denmark

[§]Ernst Ruska-Centrum and Peter Grünberg Institut, Forschungszentrum Jülich, D-52425 Jülich, Germany

Ⓢ *Supporting Information*

ABSTRACT: Single-crystalline porous CeO₂ nanocrystals, with sizes of ∼20 nm and pore diameters of 1−2 nm, were synthesized successfully using a hydrothermal method. Using electron tomography, we imaged the three-dimensional structure of the pores in the nanocrystals and found that the oriented aggregation of small CeO₂ nanoparticles resulted in the growth of CeO₂ nanocrystals with an irregular truncated octahedral shape and pores extending along the ⟨110⟩ directions. Oxygen vacancies were found on the crystal surfaces and internal walls of the pores by scanning transmission electron microscopy and electron energy-loss spectroscopy. The oxygen vacancies might play an important role in oxygen diffusion in the crystals and the catalytic activities of single-crystalline porous CeO₂ structures.
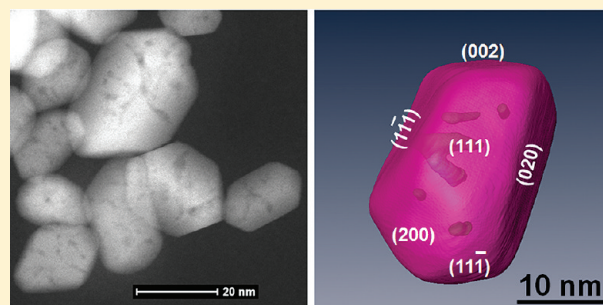
1. INTRODUCTION

Porous materials offer important technological applications in sensing, drug delivery, catalysis, and separation because both their surfaces and bulks are accessible to reactant atoms and molecules.[1] Traditionally, ordered micro- and mesoporous materials can be prepared by the surfactant-template method to create regular cavities.[2,3] These porous structures can be further employed as hard templates for the synthesis of other porous materials with the same symmetry as the original template.[4,5] An etching method is used to form some nonordered porous materials, such as Raney nickel or porous silicon.[6−9] In some cases, holes can also be created in the existing crystalline structures by substitution of different-sized elements.[10] Occasionally, cavities can be formed in the catalytic particles after calcination through agglomeration of the nanosized particles.[11] In most cases, the frameworks of porous materials are amorphous[2] or made up of the integration of randomly oriented nanoparticles.[4,5,9]

There are few reports of the synthesis of nanometer-sized single-crystalline porous materials, partially because the pores are refilled easily by highly mobile surface atoms at the nanoscale during preparation and partly because of the collapse of the unstable porous structure during crystallization at high temperature. Moreover, determining porous structures at the atomic scale and understanding the formation mechanism of the pores in nanometer-sized crystals are great challenges because of the lack of proper characterization techniques. Fabricating and understanding the structures of porous single crystals is not trivial, as the structural discontinuity caused by the pores breaks the symmetry of crystals, thus significantly affecting their mechanical, ion-conductive, and luminescence properties and resulting in different performance of the materials.[6,7]

Herein, we report the synthesis of single-crystalline porous ceria (CeO₂) nanoparticles using the hydrothermal method without any surfactants or templates. CeO₂ is an important oxide material with the face-centered cubic (fcc) fluorite structure. The ease with which the redox state of Ce can change between 4+ and 3+ and the high mobility of oxygen species in bulk CeO₂ make it an important material for multiple applications. Examples are UV absorbers; promoters in commercial catalysts to reduce emissions of CO, hydrocarbons, and NOₓ from automobile exhausts; and oxygen-ion conductors in solid fuel cells.[12−16] Our single-crystalline porous CeO₂ nanoparticles, which have not been reported before, are not only a valuable addition to the CeO₂ family of nanostructured morphologies, but also provide direct information on understanding the nucleation, growth, and self-assembly of CeO₂ nanoparticles in solution through a comprehensive analysis of the structures and orientations of the pores.

2. EXPERIMENTAL SECTION

2.1. Synthesis of Porous Nanocrystals. Porous CeO₂ nanocrystals were synthesized by a hydrothermal method, in which

1 mmol of $Ce(NO_3)_3 \cdot 6H_2O$ and 3 mmol of NaOH were mixed with 30 mL of ethanol with PVP[polyvinylpyrrolidone (PVP), 30 g/L, molecular weight 30000] and transferred to a 50 mL stainless steel atom reactor. The mixture was heated in an oven at 200 °C under autogenous pressure for 24 h. The resulting pristine 4–6-nm octahedral CeO_2 particles were washed with ethanol and water. The washed CeO_2 product was dispersed in 30 mL water with a few drops of concentrated HNO_3. Porous CeO_2 nanoparticles were obtained after the solution received an additional 24 h of hydrothermal treatment at 200 °C.

2.2. Characterization. One drop of solution containing the synthesized particles was dropped onto a transmission electron microscopy (TEM) grid coated with a layer of carbon film. Structural analysis and three-dimensional electron tomography of the CeO_2 nanoparticles were conducted using an FEI Titan 80-300 S/TEM (scanning/transmission electron microscopy) operated at 300 keV. It was equipped with a high-angle annular dark-field (HAADF) detector, a probe aberration corrector, and a single-tilt tomography holder. A total of 71 HAADF-STEM images were collected over a tilt range from $-70°$ to $70°$ with 2° tilt steps. Stage tilting and image acquisition were performed automatically by the FEI Xplore-3D tomography program, whereas tracking and refocusing of the area of interest were carried out manually to shorten the total acquisition time. The images were acquired with a magnification of 710 000×, giving an image sampling of 0.17 nm per pixel. The acquisition time for one image of size 1024 × 1024 pixels was 24 s. The final tilt series was aligned using a cross-correlation method and reconstructed by the simultaneous iterative reconstruction technique (SIRT, 50 iterations) using Inspect3D software, and the reconstructed three-dimensional volume was visualized with Amira 4.1.

Electron energy loss spectroscopy (EELS) was performed in STEM mode with a corrected probe size of about 0.2 nm. The convergence angle and collection angle were around 25 mrad, and the acquisition time for each spectrum was 5 s. The dispersion was set at 0.5 eV per pixel so that the O K and Ce M edges could be included in one spectrum. A larger camera length (128 mm) was used to acquire high-resolution images with reasonable contrast, whereas a small camera length (38 mm) was used to record spectra with the maximum signal. The secondary electron background beneath the M edges was fitted using the standard power law, and the M5 and M4 peaks were integrated individually using DigitalMicrograph software (Gatan).

3. RESULTS AND DISCUSSION

In Figure 1a, a high-angle annular dark-field scanning transmission electron microscopy (HAADF-STEM) image shows typical CeO_2 nanocrystals with particle sizes ranging from 15 to 25 nm. The spacings of the diffraction rings (inset, Figure 1a) are consistent with the cubic fluorite structure of CeO_2. HAADF-STEM images are dominated by mass–thickness contrast and are much less sensitive to diffraction contrast and Fresnel fringes.[17,18] As a result, 1–2-nm-sized pores and channels are clearly visible in the CeO_2 nanoparticles, even when they overlap each other (see Figure S1, Supporting Information). Atomic-resolution STEM images confirmed that the porous CeO_2 nanoparticles were single crystals with no twins or stacking faults. Interestingly, careful examination of the high-resolution STEM images revealed that pores in the CeO_2 nanoparticles were not randomly distributed but, rather, were aligned along certain directions. For instance, Figure 1c shows a particle imaged close to the $[1\bar{1}0]$
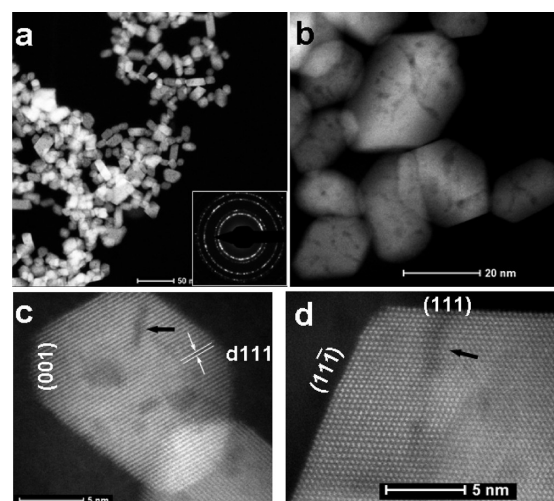

Figure 1. HAADF-STEM images of porous CeO_2 acquired at (a) low magnification, (b) high magnification, (c) atomic resolution, and (d) atomic resolution viewed along the $[1\bar{1}0]$ zone axis. A selected-area diffraction pattern is shown in the inset in panel a.

direction in which two truncated {001} surfaces, four {111} surfaces, and {111} lattice fringes (spacing 0.31 nm) are visible. One pore with a diameter of 0.95 nm is parallel to the {001} plane. A 1.2-nm-wide channel was observed to be parallel to the $(11\bar{1})$ plane in another particle (indicated by an arrow in Figure 1d). However, conventional TEM images show only two-dimensional projections of three-dimensional particles; it is thus difficult to identify the crystallographic orientation and position of the pores from a single TEM image.[19–27] Therefore, we conducted a detailed analysis of the three-dimensional shape and morphology of porous CeO_2 using electron tomography.

Figure 2 shows a three-dimensional reconstruction of one single-crystalline porous CeO_2 nanoparticle. Segmentation was used to identify the surface of the particle and the outline of individual pores by automatic selection of the threshold values of the crystal and the pores, and subsequent manual touchup was applied to remove as much as possible of the missing wedge artifacts. Six pores with various lengths can be observed. Their diameters were measured from the slice through the reconstruction shown in Figure 2c and were found to be 1.50, 1.47, 1.28, 1.34, 1.37, and 1.01 nm, respectively, for pores 1–6. Pores 3 and 4 extend from the center to the $(1\bar{1}1)$ surface, whereas the others are embedded in the particle. Successful imaging of pores as small as 1 nm indicates that the resolution of the reconstructed volume is around 1 nm or better. Surface rendering of the reconstructed structure revealed that the particle has an irregular truncated octahedral shape terminated with six truncated {001} facets and eight {111} facets, in agreement with the morphology found before by our group.[28] Measurements from the tomogram showed that the volume of the octahedra was 8232 nm^3. The pore volume fraction of this particle was (1 ± 0.25)%, with the error being estimated from ref 26.

In addition to positions of the pores, the crystallographic orientation of each pore could also be determined from the three-dimensional reconstruction by tilting the tomogram until the pore was end on. It was found that pores 2, 4, and 5 were oriented along [101], making them parallel to the (010), $(11\bar{1})$, and $(1\bar{1}\bar{1})$ planes (Figure 2g). Pores 1, 3, and 6 had their long axis along $[\bar{1}10]$, so that they were parallel to the (001), (111), and $(11\bar{1})$
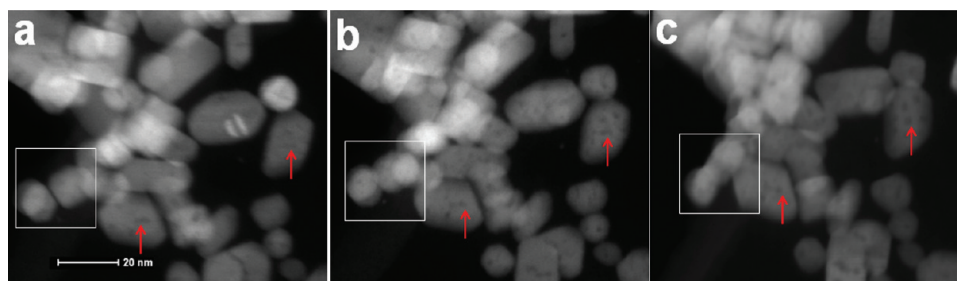
Figure 2. Reconstructed three-dimensional volume of a CeO₂ particle viewed from different directions: (a) Overview of the particle, (b) pores highlighted in green, (c) $x-y$ slice projected over a thickness of 0.17 nm, (d) isosurface-rendered view revealing the irregular octahedral shape, (e) schematic drawing of the structure. (f–j) Particle viewed along (f,g) [101], (h,i) [$\bar{1}$10], and (j) [10$\bar{1}$].

Figure 3. Schematic diagrams showing how the aggregation of particles can generate holes aligned along the ⟨110⟩ directions.

planes. Thus, in all cases, the orientations of the pores inside the crystal were not random but along the ⟨110⟩ directions and parallel to both the {001} and {111} families of planes. A video available in the Supporting Information shows the advantage of visualizing the crystal in three dimensions.

Structural and morphological studies using electron tomography can reveal the growth mechanism of the pores. In the first hydrothermal process, 4–6-nm CeO₂ nanocrystals were synthesized with a regular truncated octahedral shape, having large exposed {111} surfaces and small {001} facets at the corners because of the lower surface energy of the {111} planes.[28,29] The edges of the octahedron were along the ⟨110⟩ directions. Washing the particles with ethanol and water removed the surfactants from the surface. Without the hindrance of the PVP molecules, the octahedral CeO₂ nanocrystals tended to aggregate with their common {111} or {001} surfaces in contact, to decrease the exposed surface area and reduce the total surface energy.[30–34] The oriented aggregation and subsequent hydrothermal treatment in water led to the nucleation of larger and irregular octahedral CeO₂ nanoparticles.[28]

Because the CeO₂ assembly blocks were truncated octahedra with surface defects, spaces were left between the particles after self-assembly. Two typical examples are demonstrated in Figure 3. In Figure 3a, pairs of particles A, B and B, C share a common {111} surface, whereas particles A and C are connected by a {001} plane. A pore is generated along the edge of the octahedron, with its axis along the ⟨110⟩ direction. In Figure 3b,

one channel is formed by the aggregation of three particles through their {111} surfaces only. Thus, the occurrence of oriented attachment between the {111} surfaces results in the formation of pores along the ⟨110⟩ edges. Some longer pores in crystals are expected to be formed by oriented aggregation of larger-sized as-grown crystals.

Two possible pathways are responsible for transforming the fused particles into irregular truncated porous octahedra during the second hydrothermal process: (1) diffusion of active surface species and (2) dissolution and subsequent precipitation of ions on the surface. The surface diffusion rate is quite low during the hydrothermal process. Preliminary in situ TEM annealing experiments showed that the pores were robust and did not collapse after 1 h at 500 °C, although agglomeration between particles was occasionally observed under these conditions (Figure 4). It can be inferred that the pores will not be refilled by surface atom diffusion under low-temperature hydrothermal conditions. Moreover, the low solubility of Ce(OH)₄/CeO₂ in water leads to a low dissolution and precipitation rate during the reaction.[35] Because the channels are surrounded by fused particles, the chances of solute ions colliding with the internal surface of the pores is even lower, thus leaving the nanosized pores intact during the dissolution and precipitation process.

A few porous CeO₂ particles were also found without addition of HNO₃ (Figure S3, Supporting Information), which further confirmed that the growth of porous CeO₂ nanoparticles occurs through oriented aggregation, not etching from the acid. To reveal the role of HNO₃ in the formation of porous particles, a series of controlled experiments was carried out to ascertain the relationship between the morphology of the crystals and the acidity of the solution. We found that the optimum pH for the synthesis of highly crystalline porous CeO₂ falls between 2 and 6, where a delicate balance occurs among dissolution, aggregation, and precipitation. On one hand, Ce(OH)₄/CeO₂ is a basic precipitate.[35] The increasing solubility of CeO₂ in acidic solution enhances the dissolution/precipitation of Ce ions in the solution, leading to the formation of highly crystalline particles with sharp edges. Increasing the OH⁻ concentration decreases the solubility of Ce(OH)₄, thus making it insufficient for transforming the fused particles into one crystal and resulting in the formation of only heavily aggregated particles with poor crystal qualities. On the other

Figure 4. In situ annealing of porous nanocrystalline CeO_2 particles. STEM images were recorded (a) before particles had been heated, (b) after particles had been heated in a vacuum for 1 h at 500 °C, and (c) after particles had been heated in 2.3 mbar of H_2 for an additional 1 h. The area highlighted by the white square indicates the agglomeration of two adjacent particles at 500 °C, whereas most pores that were originally inside the nanocrystals did not collapse at the same temperature (as indicated by arrows), suggesting a relatively stable pore structure and a low diffusion rate of surface atoms.
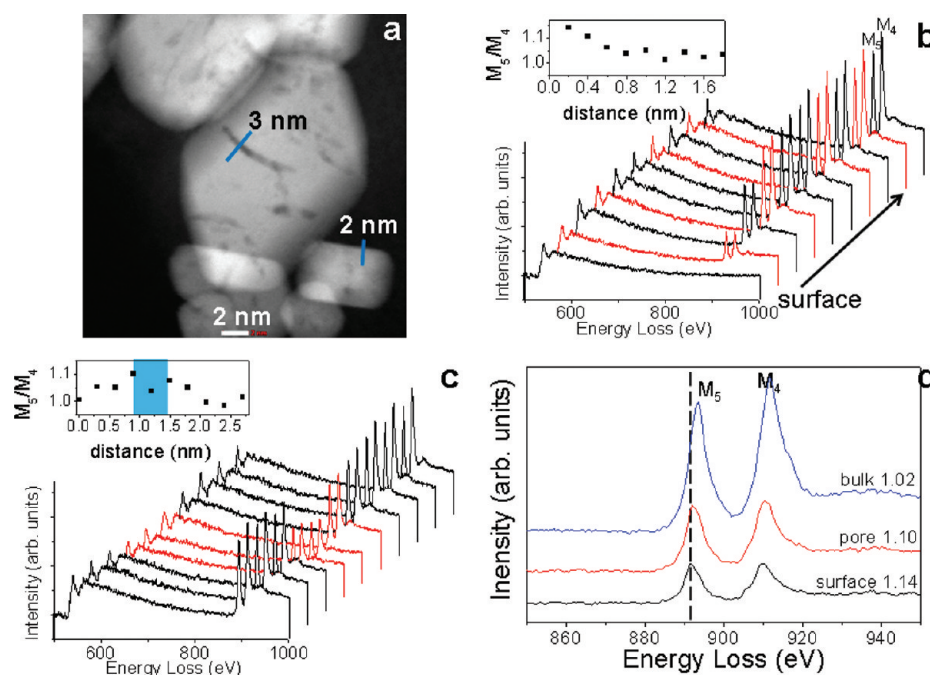
Figure 5. Chemical structure of porous CeO_2 nanocrystals determined from STEM-EELS line scans. (a) HAADF-STEM image showing the positions of the EELS line scans on two CeO_2 particles. Ten spectra obtained along (b) a 2-nm-long line across the surface of the particle and (c) a 3-nm-long line across one of the pores. The M5/M4 peak intensity ratios were calculated and are shown in the insets in panels b and c. (d) Magnified spectra showing the Ce M edges acquired at the surface, pore wall, and bulk.

hand, the oriented aggregation is strongly influenced by surface charge, such as the density of surface hydroxyl groups, in which aggregation requires dehydration of the surface hydroxyl groups on two adjacent surfaces.[36] Therefore, a highly concentrated basic solution results in severe agglomeration of the particles with high density of hydroxyl groups on the surface. An acidic environment substantially decreases the number of hydroxyl groups on the particle surface, leading to the formation of highly dispersed particles.

Single-crystalline porous CeO_2 nanocrystals not only open access to their bulk phases, but also introduce discontinuities and create oxygen vacancies inside the crystals that might affect their physical and chemical properties. In the catalytic application of CeO_2 nanocrystals, the presence of oxygen vacancies plays an important role in influencing the surface activities, diffusivities, and transport of oxygen ions from the bulk to the surface. The formation of oxygen vacancies is directly linked to the change in oxidation state

of ceria from 4+ to 3+.[37−42] We thus conducted EELS line scans across the particle surface and pore walls to explore the oxidation state of Ce and measure the oxygen vacancies.

For Figure 5b, 10 consecutive spectra were acquired from the surface to the bulk of a CeO_2 nanocrystal at 0.2-nm intervals. The oxygen K edge and cerium M edge can be seen at 532 and 883 eV, respectively. The oxidation state of cerium can be determined by measuring changes in the Ce M_{45} white lines.[37−42] A careful analysis and comparison of nine spectra showed that the surface and bulk gave distinctive spectrum profiles that could be distinguished by the onset energies, heights, and relative areas of the Ce M_5 and M_4 edges. A shift of the Ce M edge to a lower energy (by 2.5 eV) compared to the bulk spectrum (taken 1.8 nm from the surface) indicated an abundance of Ce^{3+} ions on the surface. Moreover, M_5 was found to be higher than M_4 at the surface and lower than M_4 in the bulk, showing that there was

a transformation of the Ce oxidation state from 3+ to a 4+.[40,41] The M_5/M_4 ratios at the surface and in the bulk were 1.14 and 1.02, respectively, which is in good agreement with reported changes for Ce^{3+} and Ce^{4+} ions measured by EELS.[37] It is interesting to note that the M_5/M_4 ratio gradually changed from 1.14 to 1.05 as the position of the scan moved from the surface (0 nm) into the crystal (0.6–0.8 nm). This evidence implies that, even though the bulk crystal is expected to be CeO_2 containing Ce^{4+} ions, the existence of defects, oxygen vacancies, and low-coordination sites on the surface is likely to give rise to a high concentration of Ce with the 3+ oxidation state on the surface. The concentrations of Ce^{3+} and oxygen vacancies decreased at the subsurface because of the increasing stoichiometry of CeO_2 inside the particle.

An EELS line scan across a pore is shown in Figure 5c, with spectra acquired at intervals of 0.3 nm. The fourth and sixth spectra were obtained close to the edge of the pore. The calculated M_5/M_4 ratios for these two spectra are 1.10 and 1.08, respectively, close to the value obtained from the surface. Because signal from all of the material through which the beam passed was collected, including the edge of the pore and bulk Ce^{4+} above and below the pore, a slightly smaller M_5/M_4 ratio was obtained compared to that collected from the surface where Ce^{3+} was dominant. The M_5/M_4 ratio of spectrum 5 was suddenly lower due to the dominance of the Ce^{4+} in the signal when the beam traveled through the center of the pore. Thus, ideally, thicker pores and those with edge-on walls are better candidates for accurate analysis of pore edges with EELS. As shown in Figure 5d, the fourth spectrum exhibited a profile similar to that from the particle surface. This strongly confirms the existence of Ce^{3+} ions and oxygen vacancies on the pore walls or inside the single-crystalline CeO_2 nanoparticles. We believe that the internal oxygen vacancies created by the formation of pores in the crystals might enhance the migration and transport of oxygen species from the bulk to the surface during reduction reactions.[11]

4. CONCLUSIONS

In conclusion, the three-dimensional shape and morphology of porous CeO_2 nanoparticles prepared by a hydrothermal method have been studied using electron tomography. The porous CeO_2 nanocrystals were found to have an irregular truncated octahedral shape with internal pores elongated along the ⟨110⟩ directions. The agglomeration of particles through a lattice-matched surface and subsequent low surface diffusion/ion precipitation resulted in the formation of porous structures. We believe that the crystallographic orientation of the pores and corresponding aggregation mechanism for the single-crystalline and porous CeO_2 discussed here can also be applied to other porous materials synthesized using self-assembly in solution. Also, one cannot ignore the influence of pore formation and the creation of oxygen vacancies on oxygen transport in the crystal when studying the application of CeO_2 as a catalyst in fuel cells.[11]

■ ASSOCIATED CONTENT

⑤ **Supporting Information.** Comparison between TEM and HAADF STEM images, two-dimensional image and original reconstructed volume without segmentation of the particle, STEM images of porous CeO_2 without added HNO_3, video clip showing the three-dimensional surface structure and pores of a particle in Figure 2 after segmentation. This material is available free of charge via the Internet at http://pubs.acs.org.

■ AUTHOR INFORMATION

Corresponding Author
*E-mail: m-lin@imre.a-star.edu.sg. Tel.: 65-6874 5374. Fax: 65-6874 4778.

■ ACKNOWLEDGMENT

■ REFERENCES

(1) Davis, M. E. *Nature* **2002**, *417*, 813–821.
(2) Kresge, C. T.; Leonowicz, M. E.; Roth, W. J.; Vartuli, J. C.; Beck, J. S. *Nature* **1992**, *359*, 710–712.
(3) Zhao, D. Y.; Feng, J. L.; Huo, Q. S.; Melosh, N.; Fredrickson, G. H.; Chemelka, B. F.; Stucky, G. D. *Science* **1998**, *279*, 548–552.
(4) Lara, S. C.; Ryoo, R. *Chem. Commun.* **2003**, 2138–2139.
(5) Ji, P. F.; Zhang, J. L.; Chen, F.; Anpo, M. *J. Phys. Chem. C* **2008**, *112*, 17809–17813.
(6) (a) Hochbaum, I.; Gargas, D.; Hwang, Y. J.; Yang, P. D. *Nano Lett.* **2009**, *9*, 3550–3554. (b) Zhong, X.; Qu, Y.; Lin, Y. C.; Liao, L.; Duan, X. *ACS Appl. Mater. Interfaces* **2011**, *3*, 261–270.
(7) Xu, H. L.; Wang, W. Z.; Zhu, W. *Microporous Mesoporous Mater.* **2006**, *95*, 321–328.
(8) Wang, X. D.; Ding, Y.; Li, Z.; Song, J. H.; Wang, Z. L. *J. Phys. Chem. C* **2009**, *113*, 1791–1794.
(9) Lawrence, N. J.; Jiang, K. R.; Cheung, C. L. *Chem. Commun.* **2011**, 2013–2015.
(10) Lin, M.; Zhang, J; Boothroyd, C.; Foo, Y. L.; Yeadon, M.; Loh, K. P. *J. Phys. Chem. B* **2004**, *108*, 9631–9639.
(11) Lawrence, N. J.; Brewer, J. R.; Wang, L.; Wu, T. S.; Wells-Kingsbury, J.; Ihrig, M. M.; Wang, G.; Soo, Y. L.; Mei, W. N.; Cheung, C. L. *Nano Lett.* **2011**, *11*, 2666–2671.
(12) Trovarelli, A.; de Leitenburg, C.; Boaro, M.; Dolcetti, G. *Catal. Today* **1999**, *50*, 353–367.
(13) Trovarelli, A. *Catalysis by Ceria and Related Materials*; Imperial College Press: London, 2002; pp 1–528.
(14) Steele, C. H.; Heinzel, A. *Nature* **2001**, *414*, 345–352.
(15) Zhou, K.; Wang, X.; Sun, X.; Peng, Q.; Li, Y. *J. Catal.* **2005**, *229*, 206–212.
(16) Mai, H. X.; Sun, L. D.; Zhang, Y. W.; Si, R.; Feng, W.; Zhang, H. P.; Liu, H. C.; Yan, C. H. *J. Phys. Chem. B* **2005**, *109*, 24380–24385.
(17) Loos, J.; Sourty, E.; Lu, K.; de With, G.; v. Bavel, S. *Macromolecules* **2009**, *42*, 2581–2586.
(18) Krumeich, F.; Muller, E.; Wepf, R. A.; Nesper, R. *J. Phys. Chem. C* **2011**, *115*, 1080–1083.
(19) Weyland, M.; Midgley, P. A. *Materials Today* **2004**, 32–40.
(20) Kübel, C.; Voigt, A.; Schoenmakers, R.; Otten, M.; Su, D.; Lee, T. C.; Calsson, A.; Bradley, J. *Microsc. Microanal.* **2005**, *11*, 378–400.
(21) Kaneko, K.; Inoke, K.; Freitag, B.; Hungria, A. B.; Midgley, P. A.l; Hansen, T. W.; Zhang, J.; Ohara, S.; Adschiri, T. *Nano Lett.* **2007**, *7*, 421–425.
(22) Xu, X. J.; Saghi, Z.; Gay, R.; Mobus, G. *Nanotechnology* **2007**, *18*, 225501.
(23) Bals, S.; Batenburg, K. J.; Verbeeck, J.; Sijbers, J.; Tendeloo, G. V. *Nano Lett.* **2007**, *7*, 3669–3674.
(24) van Bavel, S. S.; Sourty, E.; de With, G.; Loos, J. *Nano Lett.* **2009**, *9*, 507–513.
(25) Andersson, B. V.; Herland, A.; Masich, S.; Inganas, O. *Nano Lett.* **2009**, *9*, 853–855.
(26) Biermans, E.; Molina, L.; Batenburg, K. J.; Bals, S.; Van Tenderloo, G. *Nano Lett.* **2010**, *10*, 5014–5019.
(27) Katz-Boon, H.; Rossouw, C. J.; Weyland, M.; Funston, A. M.; Mulvaney, P.; Etheridge, J. *Nano Lett.* **2011**, *11*, 273–278.

(28) Tan, J. P. Y; Tan, H. R.; Boothroyd, C.; Foo, Y. L.; He, C. B.; Lin, M. *J. Phys. Chem. C* **2011**, *115*, 3544–3551.

(29) Sayle, T. X. T.; Parker, S. C.; Sayle, D. C. *Chem. Commun.* **2004**, 2438–2439.

(30) Wang, Z. L.; Feng, X. D. *J. Phys. Chem. B* **2003**, *107*, 13563–13566.

(31) Feng, X. D.; Sayle, D. C.; Wang, Z. L.; Paras, M. S.; Santora, B.; Sutorik, A. C.; Sayle, T. X. T.; Yang, Y.; Ding, Y.; Wang, X. D.; Her, Y. S. *Science* **2006**, *312*, 1504–1508.

(32) Hu, C.; Zhang, Z.; Liu, H.; Gao, P.; Wang, Z. L. *Nanotechnology* **2006**, *17*, 5983–5987.

(33) Yuan, Q.; Duan, H. H.; Li, L. L.; Sun, L. D.; Zhang, Y. W.; Yan, C. H. *J. Colloid Interface Sci.* **2009**, *335*, 151–167.

(34) Aneggi, E.; Llorca, J.; Boaro, M.; Trovarelli, A. *J. Catal.* **2005**, *234*, 88–95.

(35) Wu, N. C.; Shi, E. W.; Zheng, Y. Q.; Li, W. J. *J. Am. Ceram. Soc.* **2002**, *10*, 2462–2468.

(36) Si, R.; Zhang, Y. W.; You, L. P.; Yan, C. H. *J. Phys. Chem. B* **2006**, *110*, 5994–6000.

(37) Hojo, H.; Mizoguchi, T.; Ohta, H.; Findlay, S. D.; Shibata, N.; Yamamoto, T.; Ikuhara, Y. *Nano Lett.* **2010**, *10*, 4668–4672.

(38) Sharma, R.; Crozier, P. A.; Kang, Z. C.; Eyring, L. *Philos. Mag.* **2004**, *84*, 2731–2747.

(39) Fortner, J. A.; Buck, E. C. *Appl. Phys. Lett.* **1996**, *68*, 3817–3819.

(40) Wang, R. G.; Crozier, P. A.; Sharma, R.; Adams, J. B. *Nano Lett.* **2008**, *8*, 962–967.

(41) Wu, L.; Wiesmann, H. J.; Moodenbaugh, A. R.; Klie, R. F.; Zhu, Y. M.; Welch, D. O.; Suenaga, M. *Phys. Rev. B* **2004**, *69*, 125425.

(42) Turner, S.; Lazar, S.; Freitag, B.; Egoavil, R.; Verbeeck, J.; Put, S.; Strauven, Y.; Tendeloo, G. V. *Nanoscale* **2011**, *3*, 3385–3390.